Microstructure-based Nuclear Lamina Constitutive Model

Nima Mostafazadeh, Zhangli Peng*

Department of Biomedical Engineering, University of Illinois Chicago, Chicago, IL, 60607, USA

*Address correspondence to:

Dr. Zhangli Peng
Department of Biomedical Engineering
851 S. Morgan Street, 218 SEO
University of Illinois Chicago
Chicago, IL 60607, USA
E-mail: zhpeng@uic.edu; Tel: +1.312.996.8467

Abstract

The nuclear lamina is widely recognized as the most crucial component in providing mechanical stability to the nucleus. However, modeling the diverse mechanical aspects of this protein network still poses a significant challenge. We developed a constitutive model for the nuclear lamina network based on its microstructure, which accounts for the deformation phases at the dimer level, as well as the orientational arrangement and density of lamin filaments. Instead of relying on homology structure, we conducted molecular simulations to record the force-extension response of a highly accurate lamin dimer structure obtained through X-ray diffraction crystallography experimentation. Furthermore, we devised a semi-flexible worm-like chain extension-force model as a substitute for the multilinear equation, incorporating the stretching of the backbone, uncoiling of the dimer coiled-coil, and unfolding of alpha helices. Subsequently, we implemented our extension-force equation within a 2D network continuum model for the nuclear lamina and derived stress resultants. This enabled us to integrate the nuclear lamina into finite element simulations of the entire nucleus. Finally, we conducted simulations of nucleus endothelial transmigration, investigating the impact of varying network density and uncoiling constants on the critical force required for successful transmigration. The model allows us to incorporate the microstructure characteristics of the nuclear lamina into nucleus-related finite element modeling, thereby gaining insights into how laminopathies and mutations affect nuclear mechanics.

1. Introduction

The nuclear lamina is a random fibrous network of lamin protein filaments that underlies the inner nuclear membrane and interfaces with chromatin in most eukaryotic cell nuclei [1]. It has long been studied for its key role in the mechanical stability, development, and transcriptional activities of the cell [2]. The constituents of the nuclear lamina are lamin filaments, which are tetrameric assemblies of polymerized lamin isomers [3]. These isomers include lamin A (lamin A and C) and lamin B types (lamin B1 and B2), encoded by the LMNA and LMNB gene groups. Furthermore, studies have shown that lamin isomers form separate meshworks with unique functionalities and organizational structures [4]. Research suggests that the lamin A network, in particular, plays a critical role in maintaining the mechanical integrity of the nucleus during deformation events throughout its lifespan [5].

The nuclear lamina regulates or influences numerous critical biological events in cells. Therefore, structural malfunction of the nuclear lamina can lead to or facilitate severe conditions that pose significant risks to a patient's life, such as cancer and viral infections [6]. Laminopathies, a specific class of diseases, are attributed to such failures in the nuclear lamina. This category encompasses various types of muscular and skeletal dystrophies, dilated cardiomyopathy, neuropathies, and other related conditions. Additionally, it includes a rare yet complex premature aging disorder known as Hutchinson-Gilford progeria syndrome (HGPS) [7]. Certain conditions are the result of disrupted cellular proteostasis activity and the localization of mutant lamin isomers in the nuclear lamina [8]. Mutations in lamin A can alter its network-level structure and behavior, resulting in laminopathic and cancerous phenotypes [9]. In the case of HGPS, a single point mutation in the LMNA gene leads to the transcription of progerin, a protein that replaces lamin A in the nuclear lamina, and results in the formation of a dysfunctional network. [10]. In addition, It has been observed that lamin A is either upregulated or downregulated in various types of cancer [11].

These abnormalities contribute to the deterioration of nuclear biophysics, leading to a mechanically over-softened or over-stiffened response. These deviations significantly impact cell vitality and activity during dislocation through confined spaces[12-16], endothelial gaps[17] and the bloodstream[18]. The significance of these physical phenomena has sparked an interest in utilizing mathematical models and simulations to better comprehend nuclear deformation during related processes.

Numerous efforts have been made to develop models that depict the mechanical behavior of the nuclear lamina. These models have been employed in standalone simulations as well as in simulations of the entire nucleus and they encompass a wide range of approaches, including continuum linear or nonlinear shells and coarse-grained polymer models. The parameters of these models have been carefully calibrated to experimental data, ensuring their fidelity to real-world observations [19]. Research indicates that the nuclear lamina is a hierarchical, multilayered protein network characterized by its dynamic and composite assembly. Laminopathies affect cross-sectional bonds and the local concentration of lamin is directly influenced by both its nucleus transcriptive health and the mechanical deformations it experiences [20]. Consequently, mathematical models that are suitable for geometrically or chemically homogeneous structures may lack the flexibility required to investigate the variable components of the lamin network microstructure, which assertedly, are responsible for the physiological basis of mechanical deviations observed *in vivo*. As a result, subsequent attempts have been made to model the implication of the nuclear lamina as a meshwork.

Qin and Buehler developed a multi-linear relationship fitted to the *in silico* force-extension response of a homology-based lamin dimer structure and iteratively simulated a coarse-grained rectangular arrangement of filaments to capture the strain-stiffening and rupture point of the network [21]. They later simulated the same filaments in an electron-

tomography image-based network assembly [22]. These molecular dynamic simulations, aside from being time costly, present challenges when it comes to integrating with other cellular components for larger-scale simulations. A preferable approach is to develop a continuum model that takes into account the hierarchical mechanics and arrangement of the nuclear lamina and is responsive to its physical characteristics.

In the following, we elucidate the importance of the crystal structure used for our molecular dynamics (MD) uniaxial stretching simulation. We propose a mathematical model for the extension of a coiled-coil structure as a function of the applied pulling force, which bridges the low-force and high-force regimes in MD force-displacement data using a two-state kinetic model. Subsequently, we develop a constitutive model that integrates the coiled-coil model into a 2D continuous framework, enabling its implementation in finite element simulations. Additionally, to estimate the initial shear modulus and the network density, we utilize the developed coiled-coil model and Cryogenic Electron Tomography (Cryo-ET) imaging analysis, respectively. Finally, we compare the effect of various intrinsic parameters of the model in the nuclear lamina mechanics and the computed critical force in the finite element simulation of nucleus transmigration through endothelial pores.

2. Mathematical Formulation

2.1. Lamin Dimer Structure

To investigate the mechanical behavior of the dimer full-atom structure, we conducted a uniaxial stretching molecular dynamics (MD) simulation which involved applying a constant velocity of 50 Å/ps to the head end of the structure along the direction of the helical axis. Throughout the simulation, we recorded the force-displacement data associated with the stretching process. In contrast to the previously employed homology-based predicted structure of lamin A which has been used in past lamin mechanics-related models [21, 22], we utilized the experimentally derived crystal structure obtained by Ahn et al. They managed to determine the first 300 residues of the lamin A protein at a resolution of 3.2 Å, enabling us to elucidate a substantial portion of its three-dimensional structure (**Error! Reference source not found.**a) [23]. The studied domains, namely, begin with N-terminal head, followed by coil 1a, L1 linker, coil 1b, L12 linker and approximately half of the coil 2, respectively. To analyze the full dimer organization, they integrated their crystal configuration with previously reported fragments (comprising the remainder of coil 2 and the tail domain) obtained from the literature. Their findings revealed that the primary composition of a lamin dimer is predominantly comprised of coiled-coil superhelical regions. Through lateral association, dimers align their coil 1b and coil 2 regions in an anti-parallel manner to form tetramers. These tetramers then undergo polymerization to generate protofilaments, which are considered the most stable fibers in the nuclear lamina network at the highest level (**Error! Reference source not found.**b) [3]. The protofilaments overlap in apparently arbitrary alignments with respect to each other to form the nuclear lamina meshwork. In Fig. 1c, a schematic representation of a representative volume element (RVE) showcases how a sub-section of how these alignments appear. On a larger scale, the nuclear lamina forms an

irregularly intertwined meshwork of fibrous proteins along with numerous other nuclear membrane complexes, as depicted in Fig. 1d.

2.2. Lamin Dimer Extension Model

We developed a kinetic-based two-state formulation for a semiflexible filament, specifically tailored to model the extension behavior of the coiled-coil proteins such as lamin dimer in response to stretching forces. we utilized the Blundell and Terentjev extension-force equation in our modeling approach to capture the behavior of the coiled-coil [24] (Fig. 2a-I):

$$\frac{r_c}{L_c} = \left(1 + \frac{F}{L_c \mu_{0,c}}\right)\left(1 - \sqrt{\frac{k_B T}{\pi P_c (F + F_c)}}\right),$$

$$F_c = \frac{\pi^2 P_c k_B T}{L_c^2} \tag{1}$$

where subscript "c" is used to denote that the parameters for dimer end-to-end length (r_c), contour length (L_c), persistence length (P_c) and extensibility constant ($\mu_{0,c}$) are specifically defined fosr the coiled filament. To account for the behavior of highly flexible uncoiled filaments in less entropic extended dimer, we employed Petrosyan interpolation of the worm-like chain (WLC) model for flexible protein. This model effectively explained the observed trend in the high-force regime [25] (Fig. 2a-III):

$$\frac{r_u}{L_u} = \left(\frac{4}{3} - \frac{4}{3\sqrt{\alpha_2 F + 1}} - \frac{10 e^{\sqrt[4]{\frac{900}{\alpha_2 F}}}}{\sqrt{\alpha_2 F}\left(10 e^{\sqrt[4]{\frac{900}{\alpha_2 F}}} - 1\right)^2} + \frac{(\alpha_2 F)^{1.62}}{3.55 + 3.8\,(\alpha_2 F)^{2.2}} + \frac{F}{L_u \mu_{0,u}}\right),$$

$$\alpha_2 = \frac{P_u}{k_B T} \tag{2}$$

where subscript u in here indicates that same variables are defined for uncoiled dimer. A two-state transition kinetic model is used to introduce the fraction of uncoiled over coiled length (ϕ_u) under equilibrium to integrate Eq. 1 and Eq. 2 and model the uncoiling process (Fig. 2a-II):

$$r = (1 - \phi_u)\left(\frac{r_c}{L_c}\right)\left(\frac{L_c}{r_0}\right) + \phi_u\left(\frac{r_u}{L_u}\right)\left(\frac{L_u}{r_0}\right) \quad (3)$$

where r_0 is defined as the initial length of the dimer and equals to 460 Å. At equilibrium, the coiling and uncoiling rates are equal i.e., $l_c k_{c\to u} = l_u k_{u\to c}$, where l_c and l_u are length of coiled and uncoiled segments ($r = l_c + l_u$) and $k_{c\to u}$ and $k_{u\to c}$ are constants for respective transitions rates. Subsequently, one can express ϕ_u using Arrhenius equation in terms of temperature and coiling and uncoiling Gibbs free energies ($\Delta G_{c\to u}$ and $\Delta G_{u\to c}$):

$$\phi_u = \frac{l_u}{l_c + l_u} = \frac{k_{c\to u}}{k_{c\to u} + k_{u\to c}} = \frac{\frac{k_{c\to u,0}}{k_{u\to c,0}}\exp\left(\frac{-(\Delta G_{c\to u} - \Delta G_{u\to c})}{k_B T}\right)}{1 + \frac{k_{f\to u,0}}{k_{u\to c,0}}\exp\left(\frac{-(\Delta G_{c\to u} - \Delta G_{u\to c})}{k_B T}\right)} \quad (4)$$

The expression can be simplified by relating the difference in transition Gibbs energies to applied force by introducing uncoiling lengths $\Delta\Delta x$, similar to other related studies [26]:

$$\Delta G_{c\to u} - \Delta G_{u\to c} = F(\Delta x^*_{c\to u} - \Delta x^*_{u\to c}) = F\Delta\Delta x^* \quad (5)$$

By solving $\phi_u = 0.5$ for $\frac{k_{c\to u,0}}{k_{u\to c,0}}$ in terms of $\Delta\Delta x^*$ and uncoiling force $F_{0.5}$, which is the force required to uncoiled half of the coiled-coil dimer, and replacing in Eq. 4, the overall expression for ϕ_u will be:

$$\phi_u = \frac{exp\left(\frac{(F - F_{0.5})\Delta\Delta x^*}{k_B T}\right)}{1 + exp\left(\frac{(F - F_{0.5})\Delta\Delta x^*}{k_B T}\right)} \quad (6)$$

The Savitzky-Golay filter is employed to smoothen the raw force-displacement data before applying the non-linear least-squares method to fit the parameters. In order to minimize the number of independent variables in each fitting session, the data is segmented into three batches. The first batch (initial stiffening regime) is fitted to Blundell and Terentjev model for L_c, P_c, and $\mu_{0,c}$,while the last batch (final stiffening regime) is fitted to the Petrosyan interpolated relationship for L_u, P_u, and $\mu_{0,u}$. Using the known coiled and uncoiled

filament model parameters as a reference, the uncoiling transition constants ($\Delta\Delta x^*$ and $F_{0.5}$) are fitted to the entire dataset, thereby quantifying all the model parameters (Fig. 2b).

2.3. Nuclear Lamina Microstructure-Based Constitutive Model

Studies have demonstrated that the lamin A network exhibits a loose but highly dense lamin meshwork, which responds viscously to mechanical strain. On the other hand, the lamin B network forms a less dense crosslinked structure, displaying elastic behavior [20, 27]. Consequently, in deformations occurring over small timescales, the network's topology is not anticipated to undergo significant reorganization, and sliding effects are not expected to dominate even at considerably high extensions of lamin filaments [22]. Given the above considerations, it is reasonable to assume that the network deforms affinely under lower time scale biologically relevant deformations.

Under the affine assumption, the extension x of lamin dimer, oriented at an angle θ with respect to local coordinates, is related to principal stretch ratios (λ_1 and λ_2) of deforming plane that contains it through following relation:

$$x = \frac{r}{r_0} = \sqrt{{\lambda_1}^2 \cos^2\theta + {\lambda_2}^2 \sin^2\theta} \tag{7}$$

We deduced the structural properties of our network model, including the total number of dimers, using Cryo-ET image of nuclear lamina as presented in the work by Turgay et al. [28] and incorporated their analysis of filament lengths in our research. We selected the image they provided (Fig. 1d) as a RVE for the entire nuclear lamina network and further deconstructed the structure into rigidly attached dimers. Thus, the total network energy for an RVE of known dimensions can be expressed as follows:

$$E_{RVE} = \sum_{k=1}^{M} E_k \tag{8}$$

where M is the total number of dimers in the RVE. To calculate the total energy, we organized the dimers into multiple sets based on specific characteristic orientations. Under

the assumption of uniform randomness in filament orientation in vivo, we assigned an equal number of dimers to each set:

$$E_{RVE} = \sum_{i=1}^{n}\sum_{k=1}^{m_i} E_i = \sum_{i=1}^{n} m_i . E_i = \frac{M}{n}\sum_{i=1}^{n} E_i \tag{9}$$

where n is the number of characteristic orientations and m_i is the number of dimers in the RVE with orientation i. The energy density function of the RVE (W_{RVE}) is determined by dividing the E_{RVE} by its rested area (A_0). By establishing a relationship with the initial network density (ρ_0), we expressed the total number of dimers and RVE rested area as follows:

$$A_0 = \frac{M}{\rho_0} \tag{10}$$

The internal energy increment in a filament (∂E) is equivalent to the work needed to gradually stretch it ($F.\partial r$). Consequently, the stress resultants of the RVE for two principal directions have been solved analytically:

$$\tau_a = \frac{1}{\lambda_b}\frac{\partial W_{net}}{\partial \lambda_a} = \frac{1}{\lambda_b}.\frac{1}{A_0}.\frac{M}{n}.\sum_{i=1}^{n}\frac{\partial E_i}{\partial \lambda_a} = \frac{1}{\lambda_b}.\frac{\rho_0}{n}.\sum_{i=1}^{n} F.\frac{\partial r}{\partial \lambda_a} \tag{11}$$

In an axisymmetric 2D scheme, $a, b \in \{1, 2\}$ and $a \neq b$, therefore:

$$\tau_1 = \frac{\lambda_1}{\lambda_2}.\frac{\rho_0 r_0}{n}.\sum_{i=1}^{n} F.\mathrm{x}^{-1}.\cos^2\theta_i \tag{12}$$

$$\tau_2 = \frac{\lambda_2}{\lambda_1}.\frac{\rho_0 r_0}{n}.\sum_{i=1}^{n} F.\mathrm{x}^{-1}.\sin^2\theta_i \tag{13}$$

The membrane tension, shear stress resultant and shear modulus of the RVE are then derived respectively as:

$$\tau_m = \frac{\tau_1 + \tau_2}{2} = \frac{1}{2\lambda_1\lambda_2}.\frac{\rho_0 r_0}{n}.\sum_{i=1}^{n} F.\mathrm{x} \tag{14}$$

$$\tau_{shear} = \frac{\tau_1 - \tau_2}{2} = \frac{1}{2\lambda_1\lambda_2}.\frac{\rho_0 r_0}{n}\sum_{i=1}^{n} F.\mathrm{x}^{-1}.(\lambda_1^2\cos^2\theta_i - \lambda_2^2\sin^2\theta_i) \tag{15}$$

$$\mu = \frac{2\tau_{shear}{\lambda_1}^2{\lambda_2}^2}{{\lambda_1}^2 - {\lambda_2}^2} = \lambda_1\lambda_2.\frac{\rho_0 r_0}{n}.\left(\sum_{i=1}^{n} F.\mathrm{x}^{-1} + \frac{\lambda_1^2 + \lambda_2^2}{\lambda_1^2 - \lambda_2^2}\sum_{i=1}^{n} F.\mathrm{x}^{-1}.\cos 2\theta\right) \tag{16}$$

Fig. 2c graphs the membrane tension against the principal stretch ratios λ_1 and λ_2, after substituting Eq. 3 in Eq. 13.

3. Results

3.1. Force-Extension Curve

The force-extension data of the lamin A dimer exhibits striking similarities to those of macromolecules with common structural characteristics, such as vimentin [29], myosin [30], and double-stranded DNA [31], which can be attributed to the presence of shared features, including coiled-coils and extended helical motifs. On this account, all of these molecules exhibit similar stretching regimes (Fig. 2a), characterized by an initial rise, followed by a plateau, and concluding with a final rise. During the initial rise phase, the coiled-coil body harbors significant entropic energy, which is subsequently converted into mechanical work as the molecule is stretched, and this conversion continues until the entire backbone roughly aligns with the direction of the applied force. At this juncture, the dimer initiates the process of uncoiling, leading to a distinctive phase of constant force deformation: an extension phase specific to macromolecule strands in coiled-coil setup [32]. Following the uncoiling of the dimer into two monomers, the alpha helices undergo a transition to unfold into beta sheets. As the backbone becomes increasingly enthalpic, the required force for stretching it begins to increase. Collectively, these processes constitute the final rise phase [30]. Sapra et al. captured similar deformation levels by performing atomic force microscopy (AFM) indentation on single lamin filaments in situ, confirming the significance of coiled-coil compartment in lamin dimer [22].

Flexibility of protein conformations are compared by the ratio of their contour length (L) and persistence length (P), which under Brownian fluctuations is related to bending rigidity of the chain (B) by $P = \frac{B}{k_B T}$, where k_B is the Boltzmann constant and T is absolute temperature. [33]. The comparable contour and persistence length in undeformed lamin dimer

guarantees just enough bending rigidity to conserve rod-like structure[34]. Under a largely acceptable range, this state is known as semi-flexibility. Since beta-sheets are more flexible than alpha-helices [35, 36], as the protein unfolds, the persistence length of filament falls drastically behind its contour length and the whole protein destines to act flexible. Worm-like chain model fits suitable to describe mechanics of both semi-flexible and flexible filaments with finite bending rigidity. The model is a continuum approach to evaluate bending energy of a filament based on local curvature under Brownian fluctuations, that is:

$$E_b = \frac{B}{2}\int_0^L \kappa ds \tag{17}$$

where κ is local curvature at arc point s. Providing the conditions by which the equation is solved, distinct force-extension curves can be fitted to different stages of MD data. By fitting the Blundell and Terentjev semiflexible filament model to the initial stiffening regime, we obtained a persistence length ($P_c \approx 160$ nm) within the range reported in the literature [28]. Notably, the fitted persistence length is larger than the contour length ($L_c \approx 50$ nm), indicating the semi-flexible nature of this phase. The analysis of the fitted persistence lengths reveals that the entropic coiled dimer exhibits a substantially higher persistence length compared to the uncoiled extended protein ($P_u \approx 1$ A°). The extensibility constant carries distinct meanings for the coiled and uncoiled stiffening regimes. For the former ($\mu_{0,c} \approx 50{,}000$ pN/um), it represents the extension of non-coiled regions, whereas for the latter ($\mu_{0,u} \approx 700{,}000$ pN/um), it characterizes the stretching of bonds in beta-sheets.

3.3. Estimating Initial Network Density and Initial Shear Modulus

To estimate the density of lamin dimers in the nuclear lamina ρ_0, we utilized the image analysis performed by Turgay et al. with Cryo-ET images of the nuclear lamina [28]. Table 1 displays the distribution of lamin filaments with different lengths, extracted from their imaging data. Given the imaged area of 1.4 μm × 1.4 μm (Fig. 1d):

$$\text{Total number of lamin dimers} = \frac{2\sum_{i=1}^{12}\big(\text{length(i)}\big) \times \big(\text{frequency(i)}\big)}{r_0} \approx 3557$$

Where factor 2 is to accommodate for tetrameric cross-section of protofilaments. Consequently, the network density is estimated as:

$$\rho_{0,e} = \frac{\text{Estimated total number of lamin dimers}}{\text{Image area}} \approx \frac{3557}{1.4^2} = 1814\,\frac{\text{dimers}}{\mu\text{m}^2}$$

An expression for initial shear modulus of the network can be only solved by assuming a linear response for the dimer as we approach to zero in the force-extension curve. By this definition, dimer acts as a Hookean spring in this asymptote with spring constant D_0:

$$E_0 = \frac{D_0}{2} r_0^2 \left(\frac{r}{r_0} - 1\right)^2 \tag{18}$$

Since the continuity of network energy expression is a requirement in this scenario, we integrate the energy of a dimer within feasible orientation range:

$$W_0^{ave} = \frac{\rho_0}{M} \cdot \frac{2}{\pi} \cdot \int_0^{\frac{\pi}{2}} E_0\, d\theta = \frac{\rho_0 D_0 r_0^2}{M\pi} \int_0^{\frac{\pi}{2}} \left(\sqrt{{\lambda_1}^2 \cos^2\theta_i + {\lambda_2}^2 \sin^2\theta_i} - 1\right)^2 d\theta \tag{19}$$

Using Eq. 19, Svetina et al. derived expressions for τ_1 and τ_2 in terms of Incomplete elliptic integrals for $\lambda_1 > 1$ and $\lambda_2 < 1$ [37]. Employing Eq. 11 and 16, a similar expression for the shear modulus can be derived. Taking the limit of linear μ with λ_1 and λ_2 approaching to 1, the resulting solution would be:

$$\mu_0 = \lim_{\lambda_1 \to 1^+, \lambda_2 \to 1^{-1}} \frac{2\tau_{shear} {\lambda_1}^2 {\lambda_2}^2}{{\lambda_1}^2 - {\lambda_2}^2} = \frac{D_0}{8} \rho_0 r_0 \tag{20}$$

For the spring constant, we simply solved the derivative of Eq. 1 at zero force:

$$\frac{1}{D_0} = \left(\frac{dr_c}{dF}\right)\bigg|_{F=0} = \frac{2P_c^2 \pi^{\frac{7}{2}} k_B T}{L_c^4} \tag{21}$$

Therefore, the initial network shear modulus can be expressed in terms of dimer mechanics as:

$$\mu_0 = \frac{1}{4}\frac{\rho_0 r_0 P_c^2 \pi^{\frac{7}{2}} k_B T}{L_c^4} \tag{22}$$

Substituting the fitting and approximated values, the estimated value of $\mu_{0,e}$ is about 20147 N/m.

3.4. Orientation

Fig. 3 illustrates the influence of the number of characteristic orientations *n* on membrane tension τ_m from Eq. 14 and shear modulus from Eq. 16 with respect to principal stretch ratios (λ_1 and λ_2). Fig. 3a serves as both a legend for the graphs and displays the symbolic representations for different values of n. The graphs show that our model is sensitive to number of characteristic orientations we choose and that both membrane tension and shear modulus are convergent as a function of *n*. Super-resolution microscopy [4, 20] shows that lamin filaments form polygon faces with mostly 3 or 4 edges and junctions with 3 or more connectivity, thus, due to structural randomness, we fixed n to be equal to 3 for consistency.

3.5. Finite Element Modeling

We constructed and simulated an axisymmetric finite element model of a nucleus transmigrating through an endothelial pore using Abaqus/Explicit. In Fig. 4a, the geometry used is depicted, with R_n representing the radius of the nucleus, R_e being the radius of the endothelial cell, and δ denoting the radius of the pore. The endothelial cell is modeled as a neo-Hookean hyperelastic body with shear modulus μ_e = 5000 Pa. The nucleus is characterized by a solid interior with neo-Hookean properties to represent the chromatin and nucleoplasm, where the shear modulus is μ_n = 500 Pa. Additionally, it has a 30 nm thick shell that represents both lipid bilayer and the nuclear lamina. The stiffness contribution of the lipid bilayer to the shell is incorporated by introducing an additional membrane tension term, $K_{LB}.(1 - \lambda_1.\lambda_2)$ where K_{LB} = 500000 pN/μm is the area modulus of the lipid bilayer. The

geometric and material values are adopted form Cao et al. [38]. We integrated the Abaqus user material definition module VUMAT to implement our model in Abaqus. A shear force is applied to the upper half of the nucleus, causing it to push through the pore. The resistance force exerted on the endothelial cell is then measured and recorded as the critical force required for successful transmigration. Fig. 4b shows the nucleus at its critical position before passing through.

3.6. Variable Density

Fig. 5 illustrates the impact of varying the network density ρ_0 on nucleus mechanics and the nuclear lamina membrane properties in transmigration simulations. In Fig. 5a, it is evident that the critical force F_c required to pass through the endothelial pore increases as the pore radius δ tightens. Furthermore, the amplitude of this trend exhibits a direct relationship with ρ_0. At network densities as low as $\rho_0 = \rho_{0,e}/4$, the nuclear lamina enters the uncoiling phase. During this stage, the stress is mainly borne by the linear hyperelastic chromatin and the elastic lipid-bilayer, leading to the mechanical contribution of the nuclear lamina becoming negligible. As the density grows, the tightening of the pore radius reflects more significantly on the F_c and nonlinear mechanics of the nuclear lamina becomes evident. In Fig. 5b, it is evident that tuning $\rho 0$ has a more significant effect on transmigration when δ is smaller.

In Fig. 5c and Fig. 5d, the maximum membrane tension τ_m achieved at the critical point (which is the point with largest resistance force and strain) is recorded and graphed for variable ρ_0 and δ. The trend is similar for both the F_c and the maximum τ_m in the nuclear lamina, as the density increase directly influences them. At low network densities, the maximum τ_m tends to remain relatively unchanged with δ, since most of the stress is transferred to the lipid bilayer and chromatin. On the other hand, Fig. 5e and Fig. 5f demonstrate that changing the network density significantly affects the maximum shear

modulus μ throughout the whole range of pore radii. However, similar to the maximum membrane tension τ_m, at low ρ_0 values, the shear modulus of the nuclear lamina remains relatively constant.

Research indicates that under high curvature conditions, the lamin B network undergoes a dilution process to accommodate and facilitate greater deformations [20]. During transmigration, the change in the network density of the lamin can act as a crucial trigger, influencing whether the nucleus aims to prohibit or facilitate the process, therefore, the network density parameter in our microstructure-based model can serve as a valuable modeling parameter in cell mechanics simulations.

3.7. Variable $F_{0.5}$ and $\Delta\Delta x^*$

Fig. 6a, Fig. 6c, and Fig. 6e demonstrate how the reduction in the uncoiling force ($F_{0.5}$) can facilitate the transmigration of the nucleus. Similarly, Fig. 6b, Fig. 6d, and Fig. 6f show that reducing the uncoiling length ($\Delta\Delta x^*$) has a similar effect on transmigration, although reducing this parameter by the same factor as $F_{0.5}$ results in a smaller change in the mechanics of the nucleus. Studies have revealed that tetrameric interactions, such as A11 and eA22, play a crucial role in stabilizing the coiled-coil domains in the dimer. Mutations in these interactions, observed in certain laminopathies, can lead to the destabilization of the lamin dimer, resulting in either softening or stiffening effects [39]. By considering the uncoiling parameters, $F_{0.5}$ and $\Delta\Delta x^*$, the impact of these mutations on nucleus-related phenomena can be studied through finite element simulations.

4. Discussion and Conclusion

We utilized a lamin A dimer structure based on X-ray diffraction crystallography to conduct a molecular dynamics simulation of protein stretching and through this simulation, we obtained the force-extension response of the dimer. We characterized deformation phases of the lamin A dimer and employed a physics-based semiflexible model to describe the pre-uncoiling mechanical behavior. For the post-uncoiling response, we fitted the data to a flexible worm-like chain interpolation model. To model the uncoiling process, we incorporated a two-state kinetic transition fraction and combined Eq. 1 and Eq. 2 to create a comprehensive coiled-coil equation, describing the extension as a function of the pulling force. After developing expressions for the stress resultants of a 2D membrane containing lamin filaments, we derived equations for the membrane tension and the shear modulus of the nuclear lamina as a function of coiled-coil model parameters, filament characteristic orientations and network density. We approximated the initial shear modulus of the network and estimated the network density using available Cryo-ET image analysis data. Subsequently, we investigated the impact of the number of characteristic orientations on the mechanics of the nuclear lamina. Finally, we constructed a finite element model to simulate nucleus transmigration through an endothelial pore. In this model, we examined the influence of varying network density, uncoiling force, and uncoiling length across a range of pore radii on the mechanics of the nuclear lamina and the minimum force required for a successful transmigration.

Our model comprehensively integrates the microstructure and network properties of the nuclear lamina, which is the most critical mechanical component of the nucleus in finite element simulations to study nucleus-related phenomena in greater detail. In the future, this model holds the potential to enhance our understanding of the interplay between chromatin

and the nuclear lamina in nucleus mechanics. Additionally, it can be used to investigate the effects of various nucleus abnormalities, such as the distinct mechanical response of progerin compared to lamin dimer and the upregulation or downregulation of lamin in different cancers, on cell mechanical function.

5. Appendix

Lamin protofilament length (nm)	Frequency of occurrence
200	10
250	36
320	59
370	32
430	34
490	22
550	12
610	5
670	4
730	1
790	1
850	1

Table. 1 Length distribution of lamin filaments from Cryo-ET image analysis [28].

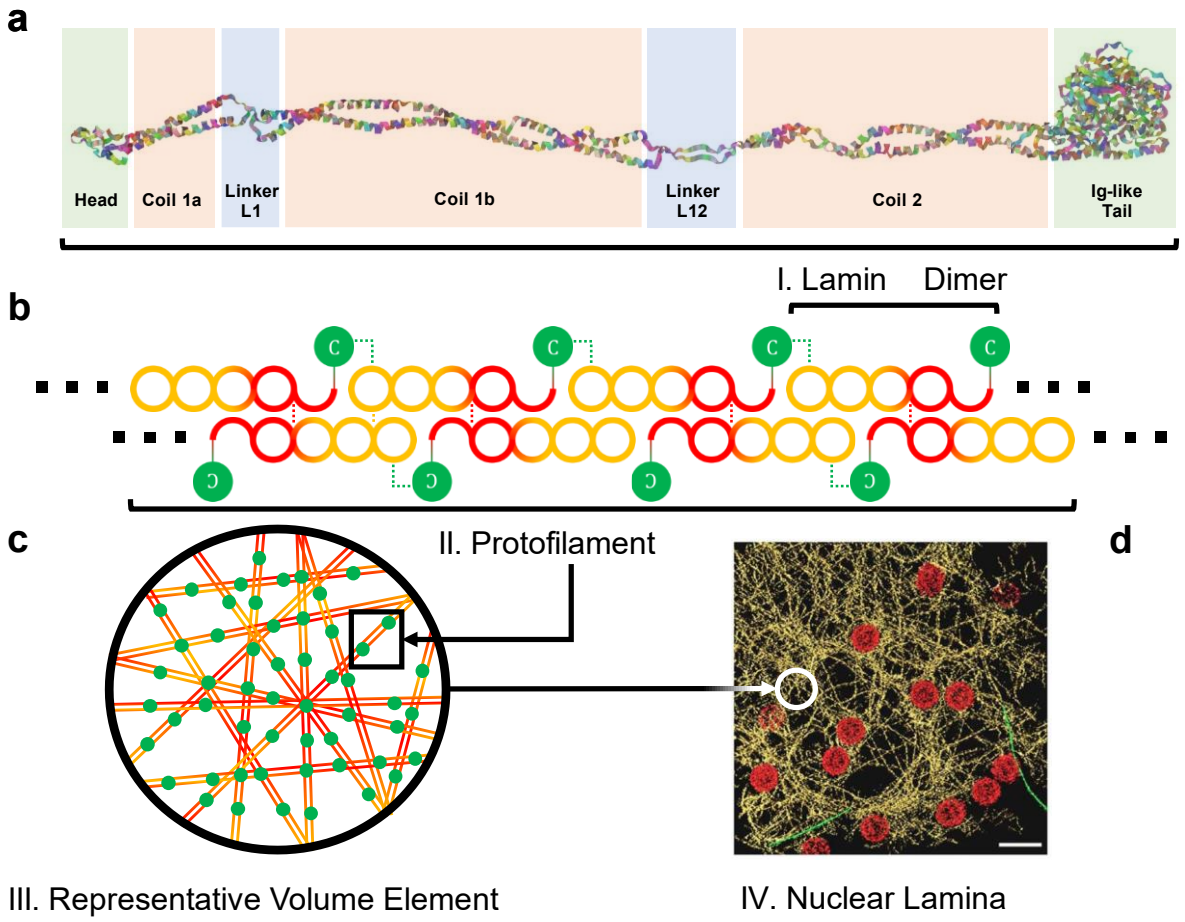

Fig. 1 Nuclear lamina hierarchical structure. (a) Lamin dimer crystal structure is shown using ribbon model with superhelical coil domains highlighted by red, linkers by blue, and head and tail residues by green. This figure suggests that the mechanics of lamin are primarily governed by its coiled-coil motifs. (b) The tetrameric and anti-parallel head-to-tail assembly of dimers gives rise to high-order protofilaments. The C-terminal immunoglobin-like domain is indicated by green circles. (c) The random alignment of protofilaments in the nuclear lamina is depicted in a representative volume element. (d) Cryo-ET-based image of nuclear lamina [28].

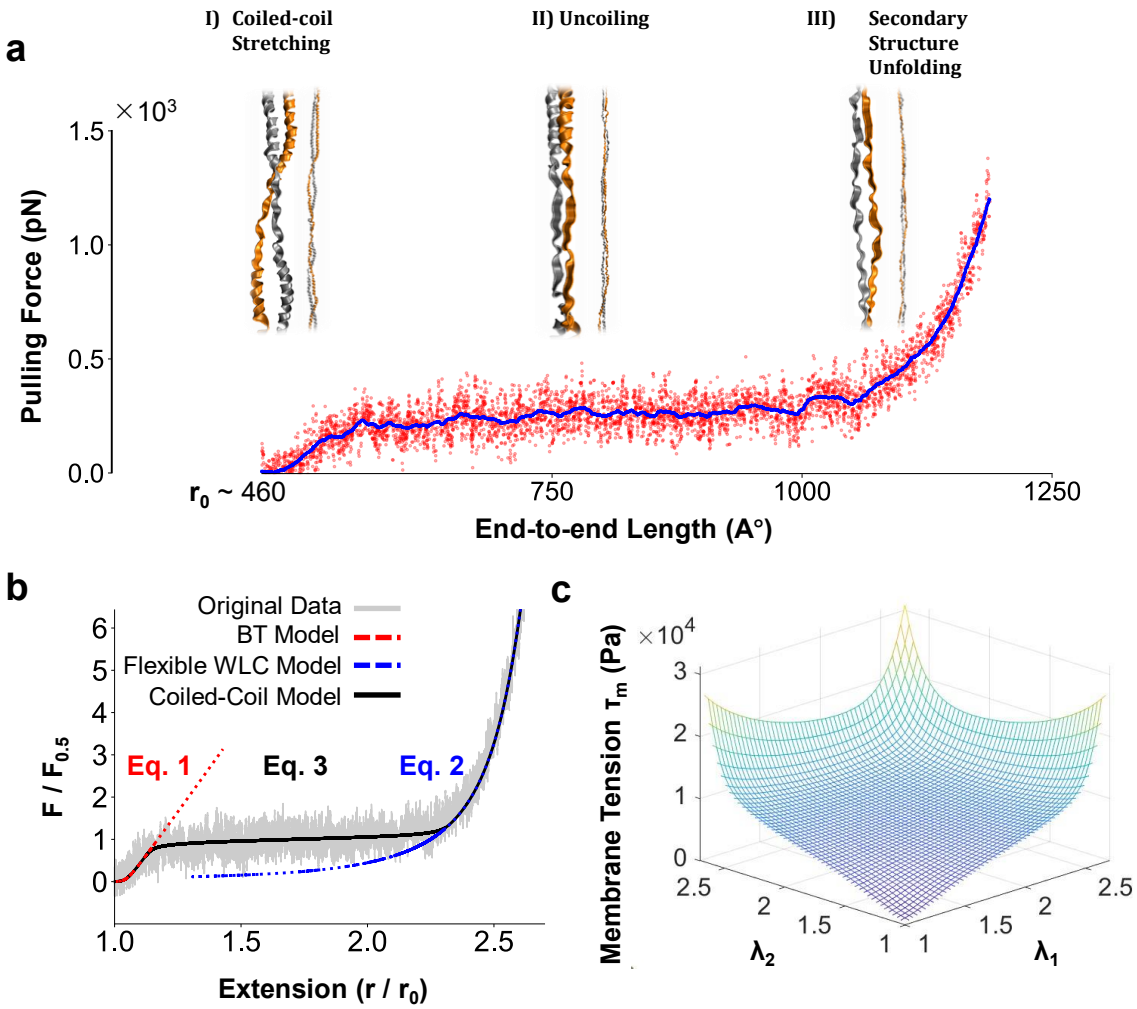

Fig. 2 Lamin dimer MD force-extension curve and coiled-coil filament modeling. (a) The figure illustrates the dimer conformations under various deformation regimes. Initially, the dimer undergoes stiffening as the coiled-coil is stretched, overcoming conformational entropy. Subsequently, uncoiling takes place at nearly constant force, followed by a final stiffening resulting from the unfolding of alpha helices. (b) Semiflexible coiled-coil model is fitted to the MD data. Given r_0 = 460 Å, the parameters for Eq. 1 were determined by fitting to the initial stiffening rise, resulting in L_c/r_0 ~ 1.06, P_c ~ 160 nm, $\mu_{0,c}$ ~ 5×10^4 pN/µm. For Eq. 2, the fitting to the final stiffening rise yielded estimated values of L_u/r_0 ~ 2.8, P_u ~ 1 A°, $\mu_{0,u}$ ~ 7×10^5. Subsequently, based on the previous estimates, $\Delta\Delta x^*$ = 1.08 A°, and $F_{0.5}$ = 203.7 pN were approximated for Eq. 3. (c) Membrane tension of the nuclear lamina network (Eq. 14) with respect to principal stretches λ_1 and λ_2.

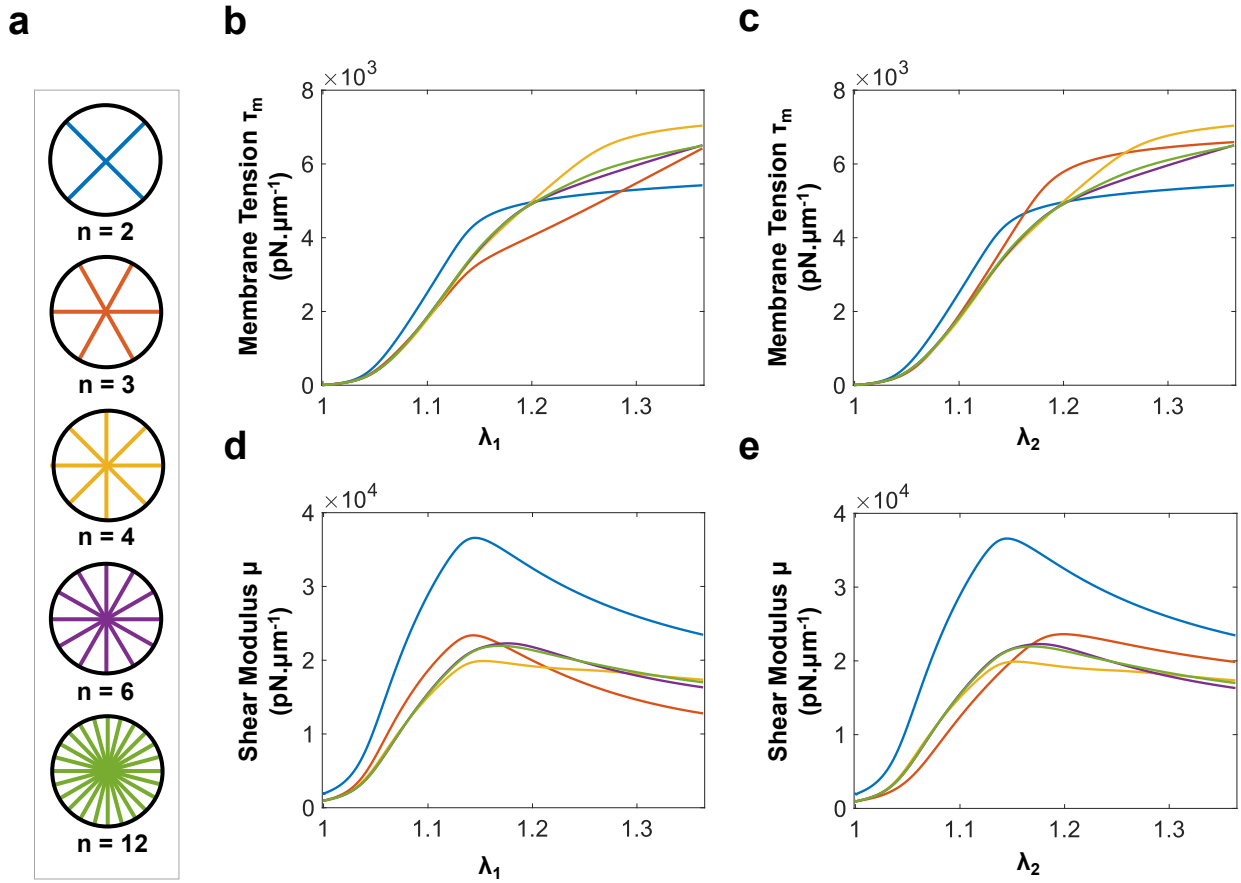

Fig. 3 The effect or number of orientations (n) on membrane tension and shear modulus. (a) The figure depicts the symbolic representation of filaments within an RVE for various values of n, where $n \in \{2, 3, 4, 6, 12\}$. (b) Membrane tension (Eq. 14) is graphed with respect to λ_1 with $\lambda_2 = 1$. (c) Membrane tension is graphed against λ_2 while $\lambda_1 = 1$. (d) Shear modulus (Eq. 16) is graphed with respect to λ_1 with $\lambda_2 = 1$. (e) Shear modulus is graphed against λ_2 while $\lambda_1 = 1$. These figures clearly demonstrate that the selection of n significantly influences the 2D membrane mechanical behavior within the specified stretch range. Moreover, they reveal that both membrane tension and shear modulus converge as a function of *n*.

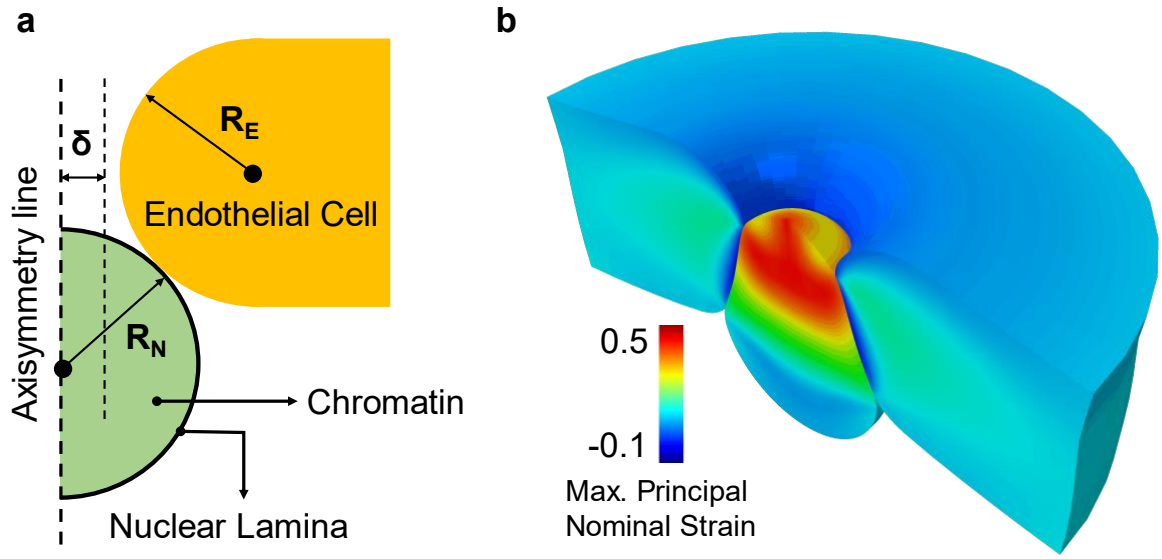

Fig. 4 Finite element modeling of nucleus transmigration through endothelial pore. (a) This figure shows a schematic of pre-deformation nucleus and endothelial cell. The radius of both nucleus and endothelial cell were fixed at $R_N = R_E = 3$ μm. The pore radius δ varies from 1 to 2.25 μm. The nuclear lamina is modeled as a shell structure that encloses the interior chromatin solid. (b) The figure showcases a post-deformation 3D cut of the nucleus passing through the endothelial pore, with maximum principal nominal strain contoured for both the nucleus and endothelial cell.

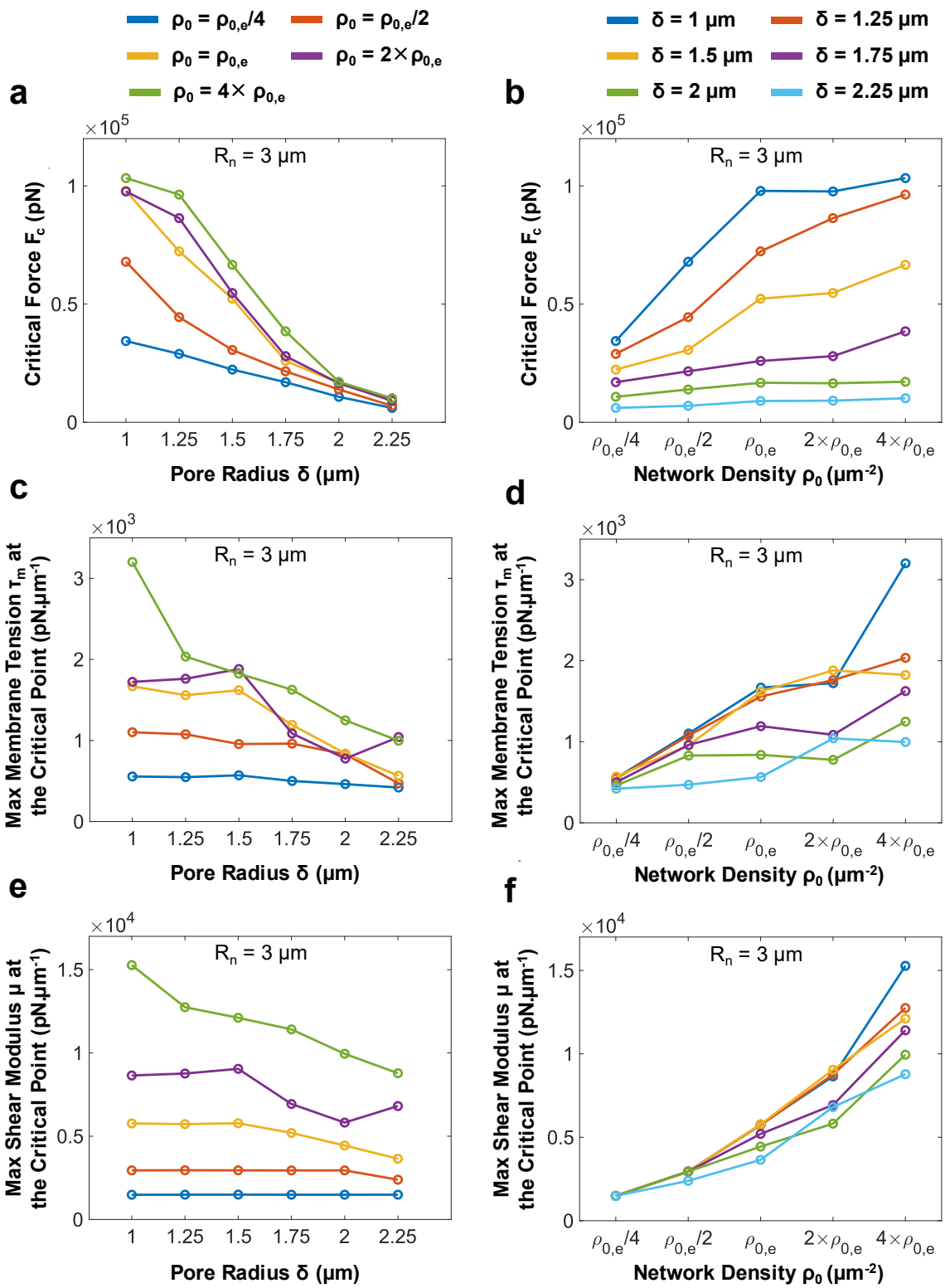

Fig. 5 Effect of network density ρ_0 in nucleus mechanics. All other parameters are fixed at their fitting values. (a) The graph displays the critical transmigration force F_c plotted against the pore radius δ, considering different multiples of $\rho_{0,e}$, with fixed nucleus radius of

R_n = 3 μm. At larger pores, the effect of density on transmigration is minimal, whereas in tighter gaps, it significantly influences the nucleus mechanics. Moreover, under light densities, the nuclear lamina undergoes uncoiling, leading to a decrease in its mechanical impact, while neo-Hookean hyperelastic chromatin becomes the dominant mechanical component. As a result, the relationship between Fc and δ becomes linear. (b) This figure illustrates F_c with respect to varying network density ρ_0 for different pore radii. This figure clearly illustrates that density has little effect on F_c at pore radii of 2.25 μm and 2 μm. However, as the pore size decreases, it begins to increase the force required for transmigration. (c) The graph illustrates the maximum membrane tension within nuclear lamina shell elements at the critical point, plotted against the pore radius for different network densities. As the density decreases, the nuclear lamina requires less tension to undergo the same strain, resulting in a decrease in the maximum membrane tension it experiences. (d) The plot illustrates the maximum membrane tension at the critical point as a function of network density for increasing pore radius. It is evident that the maximum membrane tension experienced by the network increases with its density. (e) The graph displays the maximum shear modulus of the nuclear lamina network at the critical point of transmigration, plotted against the pore radius for different network densities. At lower densities, the pore radius has minimal impact on the maximum shear modulus. However, as density increases, a nonlinear behavior in shear modulus becomes evident. (f) The plot illustrates the maximum shear modulus at the critical point, depicting its variation as a function of network density for increasing pore radius. Remarkably, the maximum shear modulus of the nuclear lamina consistently increases with density, irrespective of the pore radius.

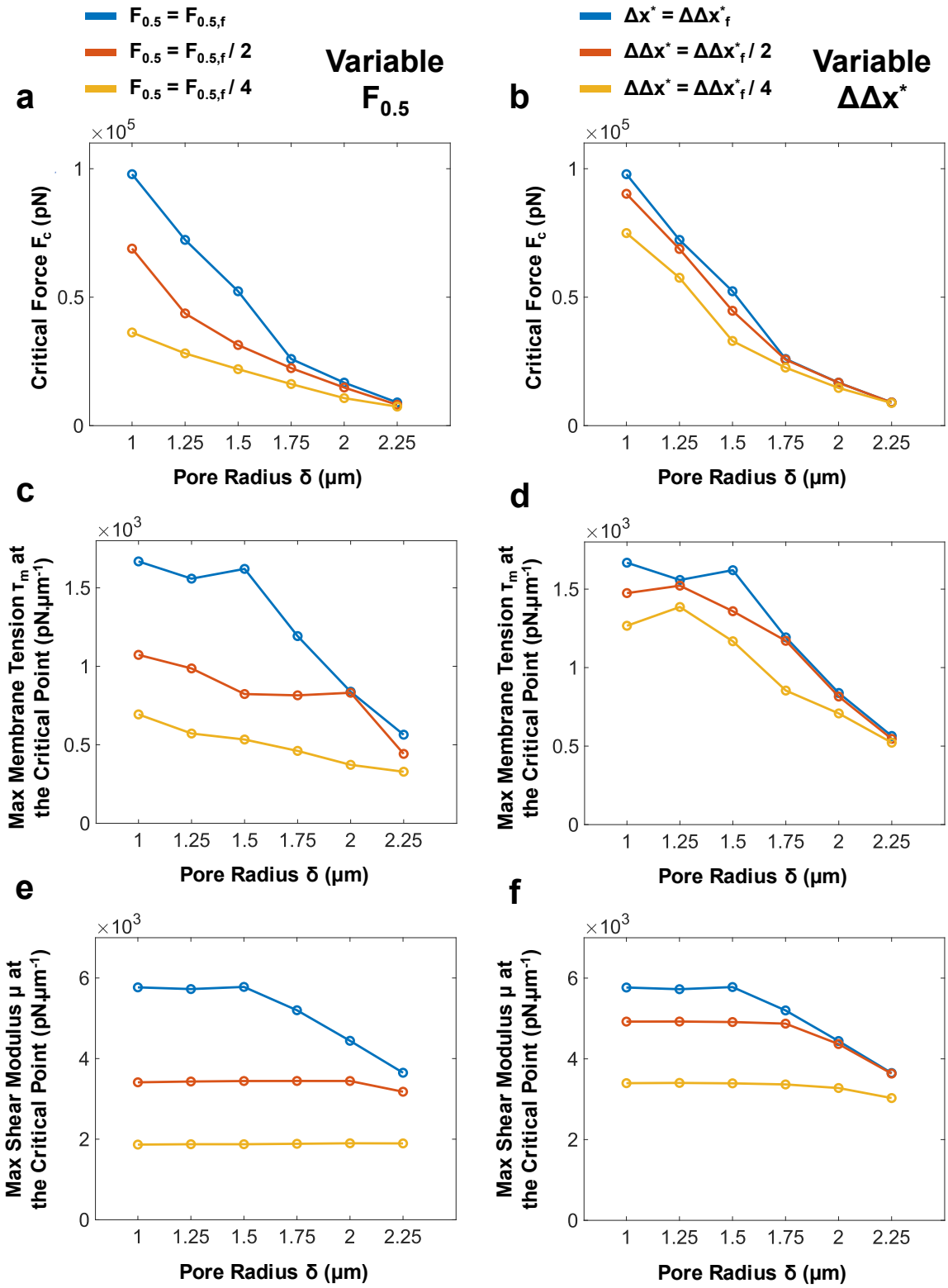

Fig. 6 The effect of lamin dimer uncoiling factors $F_{0.5}$ and $\Delta\Delta x^*$ in nucleus mechanics. All other parameters are fixed at their fitting values and density is set at $\rho_{0,e}$. Figures (a) and (b) display the critical transmigration force (*Fc*) plotted against pore radius, with one factor

reduced at a time: (a) shows the effect of reducing $F_{0.5}$, and (b) represents the effect of reducing $\Delta\Delta x^*$. Although both factors lead to a decrease in the critical force, compared to uncoiling length $\Delta\Delta x^*$, reducing the uncoiling force ($F_{0.5}$) has a more significant effect in facilitating the transmigration process. Figures (c) and (d) depict the maximum membrane tension at the critical point plotted against pore radius, considering the same parameter changes as shown in (a) and (b), respectively. The maximum membrane tension decreases significantly more when reducing $F_{0.5}$ compared to reducing $\Delta\Delta x^*$. Figure (e) and (f) demonstrate the trend of maximum shear modulus as a function of pore size, considering the same parameter changes as shown in (a) and (b), respectively. Reducing $F_{0.5}$ has a more pronounced impact, leading to more frequent uncoiling and consequent disappearance of the nuclear lamina mechanical contribution on nucleus stiffness.

References

1. Lodish, H., et al., *Molecular Cell Biology*. 2004: W. H. Freeman.
2. Wong, X., A.J. Melendez-Perez, and K.L. Reddy, *The Nuclear Lamina.* Cold Spring Harb Perspect Biol, 2022. **14**(2).
3. Turgay, Y. and O. Medalia, *The structure of lamin filaments in somatic cells as revealed by cryo-electron tomography.* Nucleus, 2017. **8**(5): p. 475-481.
4. Shimi, T., et al., *Structural organization of nuclear lamins A, C, B1, and B2 revealed by superresolution microscopy.* Mol Biol Cell, 2015. **26**(22): p. 4075-86.
5. Lammerding, J., et al., *Lamins A and C but not lamin B1 regulate nuclear mechanics.* J Biol Chem, 2006. **281**(35): p. 25768-80.
6. Stiekema, M., et al., *Structural and Mechanical Aberrations of the Nuclear Lamina in Disease.* Cells, 2020. **9**(8).
7. Worman, H.J., *Nuclear lamins and laminopathies.* J Pathol, 2012. **226**(2): p. 316-25.
8. Almendariz-Palacios, C., et al., *The Nuclear Lamina: Protein Accumulation and Disease.* Biomedicines, 2020. **8**(7).
9. Chojnowski, A., P.F. Ong, and O. Dreesen, *Nuclear lamina remodelling and its implications for human disease.* Cell Tissue Res, 2015. **360**(3): p. 621-31.
10. Dahl, K.N., et al., *Distinct structural and mechanical properties of the nuclear lamina in Hutchinson-Gilford progeria syndrome.* Proc Natl Acad Sci U S A, 2006. **103**(27): p. 10271-10276.
11. Irianto, J., et al., *The Nuclear Lamina: From Mechanosensing in Differentiation to Cancer Cell Migration*, in *Molecular and Cellular Mechanobiology*, S. Chien, A.J. Engler, and P.Y. Wang, Editors. 2016, Springer New York: New York, NY. p. 175-195.
12. Cho, S., et al., *Mechanosensing by the Lamina Protects against Nuclear Rupture, DNA Damage, and Cell-Cycle Arrest.* Dev Cell, 2019. **49**(6): p. 920-935 e5.
13. Krause, M. and K. Wolf, *Cancer cell migration in 3D tissue: negotiating space by proteolysis and nuclear deformability.* Cell Adh Migr, 2015. **9**(5): p. 357-66.
14. Harada, T., et al., *Nuclear lamin stiffness is a barrier to 3D migration, but softness can limit survival.* J Cell Biol, 2014. **204**(5): p. 669-82.
15. Elacqua, J.J., A.L. McGregor, and J. Lammerding, *Automated analysis of cell migration and nuclear envelope rupture in confined environments.* PLoS One, 2018. **13**(4): p. e0195664.
16. Bell, E.S., et al., *Low lamin A levels enhance confined cell migration and metastatic capacity in breast cancer.* Oncogene, 2022. **41**(36): p. 4211-4230.
17. Manley, H.R., M.C. Keightley, and G.J. Lieschke, *The Neutrophil Nucleus: An Important Influence on Neutrophil Migration and Function.* Front Immunol, 2018. **9**: p. 2867.
18. Zhao, B., M. Tang, and Y. Lv, *Shear stress regulates the migration of suspended breast cancer cells by nuclear lamina protein A/C and large tumor suppressor through yes-associated protein.* Hum Cell, 2022. **35**(2): p. 583-598.
19. Hobson, C.M. and A.D. Stephens, *Modeling of Cell Nuclear Mechanics: Classes, Components, and Applications.* Cells, 2020. **9**(7).
20. Nmezi, B., et al., *Concentric organization of A- and B-type lamins predicts their distinct roles in the spatial organization and stability of the nuclear lamina.* Proc Natl Acad Sci U S A, 2019. **116**(10): p. 4307-4315.

21. Qin, Z. and M.J. Buehler, *Flaw tolerance of nuclear intermediate filament lamina under extreme mechanical deformation.* ACS Nano, 2011. **5**(4): p. 3034-42.
22. Sapra, K.T., et al., *Nonlinear mechanics of lamin filaments and the meshwork topology build an emergent nuclear lamina.* Nat Commun, 2020. **11**(1): p. 6205.
23. Ahn, J., et al., *Structural basis for lamin assembly at the molecular level.* Nat Commun, 2019. **10**(1): p. 3757.
24. Blundell, J.R. and E.M. Terentjev, *Stretching Semiflexible Filaments and Their Networks.* Macromolecules, 2009. **42**(14): p. 5388-5394.
25. Petrosyan, R., *Improved approximations for some polymer extension models.* Rheologica Acta, 2017. **56**(1): p. 21-26.
26. Lee, J.C. and D.E. Discher, *Deformation-enhanced fluctuations in the red cell skeleton with theoretical relations to elasticity, connectivity, and spectrin unfolding.* Biophys J, 2001. **81**(6): p. 3178-92.
27. Wintner, O., et al., *A Unified Linear Viscoelastic Model of the Cell Nucleus Defines the Mechanical Contributions of Lamins and Chromatin.* Adv Sci (Weinh), 2020. **7**(8): p. 1901222.
28. Turgay, Y., et al., *The molecular architecture of lamins in somatic cells.* Nature, 2017. **543**(7644): p. 261-264.
29. Qin, Z., L. Kreplak, and M.J. Buehler, *Hierarchical structure controls nanomechanical properties of vimentin intermediate filaments.* PLoS One, 2009. **4**(10): p. e7294.
30. Root, D.D., et al., *Coiled-coil nanomechanics and uncoiling and unfolding of the superhelix and alpha-helices of myosin.* Biophys J, 2006. **90**(8): p. 2852-66.
31. Marko, J.F. and E.D. Siggia, *Stretching DNA.* Macromolecules, 1995. **28**(26): p. 8759-8770.
32. Goktas, M., et al., *Molecular mechanics of coiled coils loaded in the shear geometry.* Chem Sci, 2018. **9**(20): p. 4610-4621.
33. Broedersz, C.P. and F.C. MacKintosh, *Modeling semiflexible polymer networks.* Reviews of Modern Physics, 2014. **86**(3): p. 995-1036.
34. Schopferer, M., et al., *Desmin and vimentin intermediate filament networks: their viscoelastic properties investigated by mechanical rheometry.* J Mol Biol, 2009. **388**(1): p. 133-43.
35. Emberly, E.G., et al., *Flexibility of alpha-helices: results of a statistical analysis of database protein structures.* J Mol Biol, 2003. **327**(1): p. 229-37.
36. Emberly, E.G., et al., *Flexibility of beta-sheets: principal component analysis of database protein structures.* Proteins, 2004. **55**(1): p. 91-8.
37. Svetina, S., et al., *A novel strain energy relationship for red blood cell membrane skeleton based on spectrin stiffness and its application to micropipette deformation.* Biomech Model Mechanobiol, 2016. **15**(3): p. 745-58.
38. Cao, X., et al., *A Chemomechanical Model for Nuclear Morphology and Stresses during Cell Transendothelial Migration.* Biophys J, 2016. **111**(7): p. 1541-1552.
39. Ahn, J., et al., *Separation of Coiled-Coil Structures in Lamin A/C Is Required for the Elongation of the Filament.* Cells, 2020. **10**(1).